



# Microstructure and mechanical properties of $\text{Ni}_{1.5}\text{Co}_{1.5}\text{CrFeTi}_{0.5}$ high entropy alloy fabricated by mechanical alloying and spark plasma sintering

Igor Moravcik <sup>a,\*</sup>, Jan Cizek <sup>a</sup>, Jozef Zapletal <sup>a</sup>, Zuzana Kovacova <sup>b</sup>, Jozef Vesely <sup>c</sup>, Peter Minarik <sup>c</sup>, Michael Kitzmantel <sup>b</sup>, Erich Neubauer <sup>b</sup>, Ivo Dlouhy <sup>a,d</sup>

<sup>a</sup> NETME Centre, Institute of Materials Science and Engineering, Brno University of Technology, Technicka, 2896/2 Brno, Czech Republic

<sup>b</sup> RHP-Technology GmbH, Forschungs- und Technologiezentrum, 2444 Seibersdorf, Austria

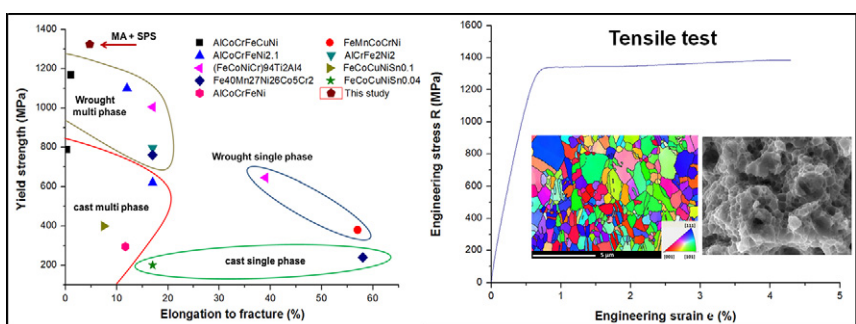
<sup>c</sup> Department of Physics of Materials, Faculty of Mathematics and Physics, Charles University, Ke Karlovu 5, Praha 2 121 16, Czech Republic

<sup>d</sup> Institute of Physics of Materials CAS, Zizkova 22, 61662 Brno, Czech Republic

## HIGHLIGHTS

- One phase FCC ultra-fine grained HEA with no porosity was produced via powder metallurgy.
- For the first time, tensile test specimens produced from SPS compacts were tested.
- The alloy exhibited excellent tensile strength of 1384 MPa, superior to HEA produced by casting routes.
- Ductile fracture mode with dimple morphology has been observed on fracture surfaces.

## GRAPHICAL ABSTRACT



## ARTICLE INFO

### Article history:

Received 29 September 2016

Received in revised form 6 January 2017

Accepted 12 January 2017

Available online 16 January 2017

### Keywords:

Multi principal element alloy

Tensile strength

Fracture

Ductility

## ABSTRACT

The present work is focused on synthesis and mechanical properties evaluation of non-equiautomatic  $\text{Ni}_{1.5}\text{Co}_{1.5}\text{CrFeTi}_{0.5}$ , ductile single phase high entropy alloy (HEA) with excellent mechanical properties (bend strength  $R_{mb} = 2593$  MPa, tensile strength  $R_m = 1384$  MPa, tensile elongation to fracture of 4.01%, and elastic modulus of 216 GPa) surpassing those of traditional as-cast HEA. For the alloy production, a combination of mechanical alloying (MA) process in a planetary ball mill and spark plasma sintering (SPS) for powder densification was utilized. The tensile properties of a bulk material produced by a combination of MA + SPS are characterized for the first time. The feedstock powder and corresponding bulk material microstructure, elemental and phase composition, and mechanical properties were investigated by scanning (SEM) and transmission (TEM) electron microscopy, energy-dispersive X-ray spectroscopy (EDX), electron backscatter diffraction (EBSD), X-ray diffraction (XRD), as well as impulse excitation of vibration, Vickers microhardness and tensile and bend strength tests, respectively. The structure of the samples consisted of single-phase FCC high entropy solid solution of extremely fine-twinned grains and oxide inclusions inherited from the original powder feedstock. Dimple-like morphology corresponding to ductile fracture mode has been observed on the fracture surfaces, with crack initiation sites on the inclusions phases.

© 2017 Elsevier Ltd. All rights reserved.

\* Corresponding author.

E-mail address: [moravcik@fme.vutbr.cz](mailto:moravcik@fme.vutbr.cz) (I. Moravcik).

## 1. Introduction

In their pioneer work, Yeh et al. [1] designed an equiatomic elements alloy comprising of five elements with a simple disordered solid solution structure. Along with others like Cantor [2,3], they provided a new direction in metal alloys development; instead of using the traditional element-doped-into-base-matrix design approach, they chose multi-element systems with near equimolar ratios. This new class of materials was denominated as high entropy alloys (HEA). Over the time, a number of various alloy systems have been examined [4]. However, most of such studied systems exhibited complicated structures containing e.g. intermediate phases, thereby deriving from the original idea of one solid solution [5–7]. Such multi-phase microstructure alloys of near equimolar element ratios are now referred to as multi-principal-element alloys (MPEA). As well as HEA, these alloys are, too, being developed considering their suitability for some targeted use such as high strength or high temperature applications (where their multi-phase structure is more desirable [8,9]). In fact, Wu et al. [10] proposed that the idea of stabilization of simple solid solutions by high configurational entropy (i.e., the currently acknowledged basic HEA principle) may be wrong and highlighted more prominent role of the mixing enthalpy.

Regardless of the terminology, these new materials have attracted substantial scientific interest due to their excellent combination of properties like high strength and ductility [11,12], wear resistance [13], or e.g. fracture resistance [14]. This behavior is a result of the inherent ductile nature of solid solutions with high strength, derived from severe lattice strains present in the microstructure [4].

Despite the variety of designed and studied HEA, their tensile strength test performance was rarely documented. Due to the relative simplicity of the tests, the reported mechanical behavior of HEA mainly come from compression loading, which usually yields higher apparent strength and ductility combination [15]. To boost the application of HEA, mechanical testing that better corresponds with the stress-strain conditions of real parts in service is needed (cf. the outcomes of compression testing only). Results indicate that in general, FCC lattice HEA usually possess good tensile ductility, but their strengths are low, while BCC lattice HEA can have a high strength but rather poor tensile ductility [4].

At the present, majority of HEA is produced by the melting and casting procedure. Due to chemical or segregation phenomena, additional time and energy consuming processes like homogenization and hot working [10,16] are required to obtain the desired properties.

By utilizing powder metallurgy (PM) fabrication approach, in particular mechanical alloying (MA) of pure elemental powders and a subsequent powder densification by spark plasma sintering (SPS), it is possible to – relatively easily – obtain dense bulk materials, as proven in a number of previous studies [17–20]. There are a number of benefits resulting from this manufacturing method, such as production of nanograined materials [19,21], ease of advanced composite preparation [22,23], and no segregation problems [24]. Given these, it could be expected that the properties of PM fabricated HEA bulks have a potential of overcoming limitations encountered in the casting routes. At the moment, though, the high hardness and high strength HEA materials fabricated via PM routes usually possess very limited ductility values. This may present a problem for e.g. structural materials, where ductility is a critically important property for manufacturing of damage tolerant

structures [25]. As such, there is a need to produce HEA with sufficient ductility values, too.

According to the authors knowledge, this paper present the first systematic study reporting bend and tensile strength test behavior and fracture mechanism of HEA materials produced by a combination of MA + SPS showing strengths superior to those of as-cast bulks, while maintaining reasonable ductility (and hence promising application potential).

## 2. Experimental

The nominal composition of the investigated alloy was  $\text{Ni}_{1.5}\text{Co}_{1.5}\text{CrFeTi}_{0.5}$  (expressed in molar ratio). The particular concentration was chosen from the previous studies due to its combination of superior corrosion properties, wear resistance and high temperature strength [13,26,27]. Importantly, the alloy also inherently represents a promising material of a good combination of strength-to-ductility. Elemental powders of Cr, Co, Ni, Fe, and Ti with high purity (all > 99.5 wt%, Sigma Aldrich) were processed by mechanical alloying. The process was carried out in an in-house made EN 1.2379 (X120CrMoV 12-1) hardened tool steel vial, into which the powders were sealed together with hardened EN 1.3505 (100Cr6) steel balls (a mixture of 15 mm and 20 mm balls, 10:1 total ball to powder weight ratio) in a high purity (6.0) nitrogen atmosphere. The sealed vial was then placed in a high energy planetary ball milling (Fritsch Pulverisette 6) and dry milled at speeds of 250 rpm for 30 h. Consequently, additional 2 h of wet milling in toluene to decrease the powder particles size and to remove powder stuck to the milling media was carried out.

The ball milled powders were subsequently consolidated by SPS technology in a 50 mm-inner-diameter graphite die at 1423 K for 20 min. The sintering was performed in vacuum (residual cell pressure < 8 Pa) at a constant pressure of 30 MPa. For easy removal and reduction of a potential surface contamination, graphite foils coated with boron nitride layer were placed between the die and the powders. The sintering had been controlled by a preset heating program. The heating from RT to 1273 K was done at a heating rate of  $100 \text{ K} \cdot \text{min}^{-1}$  with 15 min dwell time at temperature of 823 K to ensure removal of organic compounds (e.g. residual toluene from the wet milling). From 1273 K to 1373 K, the heating rate was reduced to  $50 \text{ K} \cdot \text{min}^{-1}$  and further to  $20 \text{ K} \cdot \text{min}^{-1}$  in the final sintering range of 1373–1423 K to ensure the best possible densification conditions. After the sintering, the pressure from pistons and the electric current were removed and the whole setup was left to cool down to RT in the vacuum encapsulation. The resulting specimen was then a 50 mm diameter cylinder with thickness of 7 mm.

From the sintered compact, four different sample types were prepared. For SEM, EDX, EBSD, and XRD analyses, bars with dimensions  $6 \times 4 \times 4$  mm were cut, resin-mounted and metallographically polished. The SEM characterization (powders, bars, and fracture surface after the mechanical testing) was carried out using Zeiss Ultra Plus microscope at accelerating voltage of 10 kV in both secondary and backscattered electrons mode, as well as in electron channelling contrast imaging (ECCI) mode [28]. The phase composition observation (XRD) of the materials was carried out using Philips X'Pert diffractometer (40 kV) with  $\text{Cu K}_\alpha$  radiation and the 2θ range of 30–90°, followed by the spectra analysis in X'Pert High Score Plus software. Secondly, thin foil coupons were prepared for TEM (Jeol 2200FS) observation of microstructure and selected area electron diffraction (SAED) analysis. Lastly,  $22 \times 6 \times 4$  mm and  $27 \times 6 \times 4$  mm bars were cut from the samples by means of EDM (electric discharge machining) for bend strength and tensile strength testing, respectively. The 6 mm face of these samples corresponded to the direction parallel to the SPS pressing direction. The specimens for tensile strength testing were then further machined to obtain cylindrical shape with the gauge length of 12.5 mm and diameter of 3.5 mm.

Room temperature bending strength ( $R_{mb}$ ) was then measured from 6 samples using three-point bending setup (Zwick Z2020 universal

**Table 1**

Calculated HEA phase content related parameters of the investigated  $\text{Ni}_{1.5}\text{Co}_{1.5}\text{CrFeTi}_{0.5}$  alloy.

Calculated theoretical density [g.cm <sup>-3</sup> ]	δ [%]	$S_{conf}$ [J·K <sup>-1</sup> ·mol <sup>-1</sup> ]	VEC [1]	$\Delta H_{mix}$ [kJ.mol <sup>-1</sup> ]	Ω [1]
7.79	5.04	12.86	8.09	-10.74	2.22

tensile test machine), with the loading span of 18 mm and a cross-head speed of  $1 \text{ mm} \cdot \text{min}^{-1}$ . The value for work of fracture was determined according to a definition as an area under the load – deflection curve.

The tensile strength test was performed using one sample with a crosshead speed of  $0.2 \text{ mm} \cdot \text{min}^{-1}$  (i.e., strain rate of  $0.25 \times 10^{-4}$  according to EN ISO 6892 [29]; Instron 8801 testing machine) at room temperature. The differential Crussard–Jaoul analysis was performed to determine the strain hardening exponent  $n$  supposing Hollomon equation quantifying the uniform deformation of tensile curve [30]. To suppress the influence of the frame and other factors, the elongation was measured with precise extensometer attached directly to the specimen gauge length.

The elastic modulus measurement was carried out according to ASTM E 1876-09 standard [31] by impulse excitation of vibration (Grindosonic MK5i, 10 measurements). Vickers hardness measurement was carried out under a load of 300 g. The presented value is an average of 7 measurements.

### 3. Results and discussion

#### 3.1. Phase prediction

Several parameters have been proposed in the literature to predict phase composition of high entropy alloys without the need to use CALPHAD software or ab-initio calculations. Yang et al. [32] proposed enthalpy of mixing  $\Delta H_{mix}$ , configurational entropy  $\Delta S_{conf}$ , and element radii mismatch  $\delta$  as the criteria for such predictions. The respective equations for the calculation of these parameters can be found in their work [33]. According to their findings, disordered solid solutions form when  $-15 \leq \Delta H_{mix} \leq 5 \text{ kJ} \cdot \text{mol}^{-1}$  and  $\delta \leq 6.6\%$  in cases when  $\Delta H_{mix} \leq \Delta S_{conf}$ . In their calculation they further designed parameter  $\Omega$  as

$$\Omega = \frac{T_m \Delta S_{conf}}{|\Delta H_{mix}|} \quad (1)$$

where  $T_m$  is a melting temperature of the system, calculated as an average of melting temperatures of its components. If  $\Omega \geq 1$  and  $\delta \leq 6.6\%$ , the microstructure should be composed of one high entropy solid solution phase only. Zhang et al. [12] later corrected the criterion. According to their findings, single phase solid solution microstructure is formed

when  $\delta \leq 4\%$ ,  $-10 \leq \Delta H_{mix} \leq 5 \text{ kJ} \cdot \text{mol}^{-1}$  and  $\Delta S_{conf} > 13.38 \text{ J} \cdot \text{mol}^{-1}$  only. This statement was supported in several previous research studies of cast  $\text{Ni}_{1.5}\text{Co}_{1.5}\text{CrFeTi}_{0.5}$  HEA ( $\delta = 5.04\%$ ), where  $\gamma'$  ( $\text{Ni}_3\text{Al}$ ) and  $\eta$  ( $\text{Ni}_3\text{Ti}$ ) ordered intermetallic phases were identified [5,13]. From the average valence electron concentration (VEC) proposed by Guo [34], a formation of BCC or FCC solid solution can be predicted; in case of  $\text{VEC} \geq 8$  the alloys should possess FCC microstructure.

All the parameters calculated for the composition presented in this paper are summarized in Table 1. Based on the respective values for used composition (in particular,  $\delta > 4\%$ ,  $\Delta S_{conf} < 13.38 \text{ J} \cdot \text{mol}^{-1}$  and  $\Delta H_{mix} \leq -10 \text{ kJ} \cdot \text{mol}^{-1}$ ), the alloy should – according to the prediction – most likely be composed of FCC solid solution matrix phase and minor precipitated phases.

#### 3.2. Microstructural and phase evolution

The measured XRD patterns of all samples are provided in Fig. 1. The spectrum of the blended-only elemental powders is presented in Fig. 1a. In the blend, all major peaks of the five respective elements were identified. After the MA procedure (Fig. 1b), three phases were formed: one BCC phase with lattice parameter of  $2.87 \text{ \AA}$  (i.e., close to Cr and Fe) and two FCC phases with lattice parameters of  $3.52 \text{ \AA}$  and  $3.58 \text{ \AA}$ , respectively (i.e., both close to Ni). The milling process introduces extremely high concentration of defects to the powder microstructure, including vacancies, which play a major role in the diffusion process kinetics. Also, a certain amount of heat is generated, further supporting the diffusion of elements. The mechanical activation of the powders therefore probably triggered an alloying reaction during the milling process already, leading to a formation of the BCC and two FCC phases. In the milling process, elements with lower melting points usually dissolve in a matrix of higher melting points elements, as previously reported in e.g. [17,18, 35]. However, this theory was not confirmed in the presented study as the detected XRD peaks pertained to FCC solid solution close to Ni, i.e. to the element with the lowest melting point (1728 K) among the used powders. The evident peak broadening suggests either lattice distortion due to the induced strains, resulting in an increased X-ray beam scatter, or an excessive grain refinement induced by the repeated cold deformation, thereby increasing the volume of grain boundaries, triggering the same scatter effect. Due to the nature of the milling process,

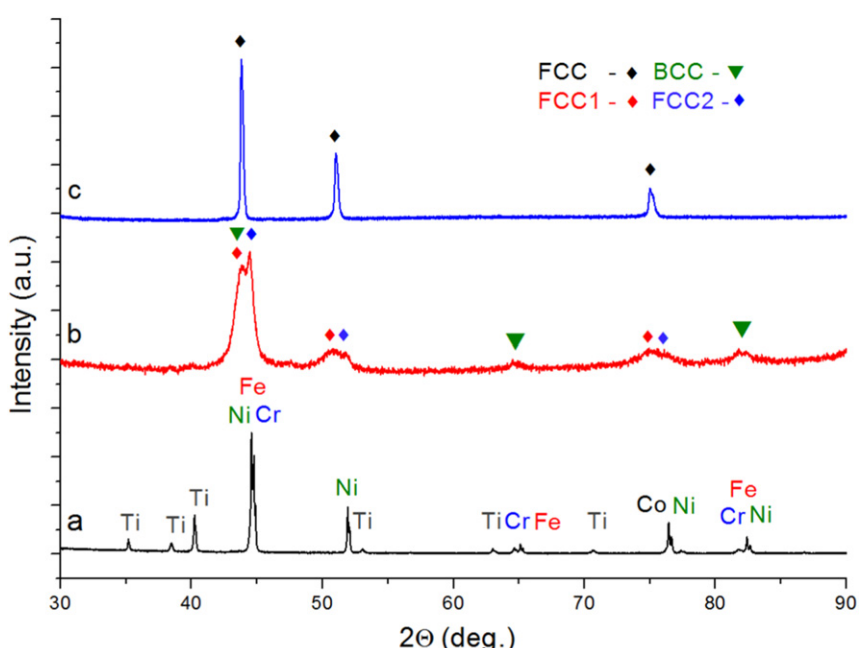


**Fig. 1.** XRD patterns of (a) blended powder feedstock (b) mechanical alloyed powder (c) SPS compacted alloyed powder.

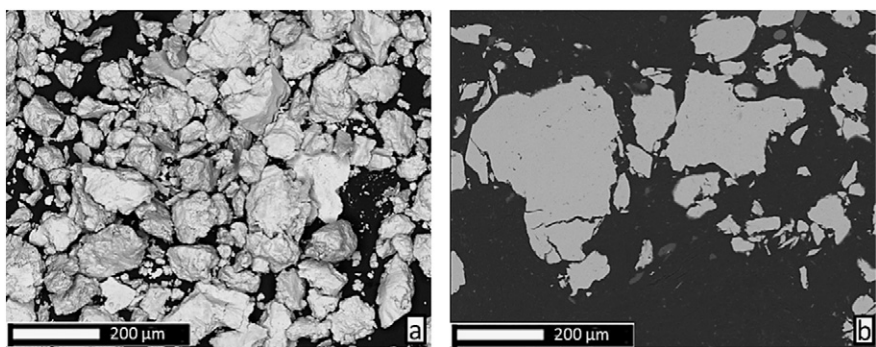


**Fig. 2.** Mechanically alloyed  $\text{Ni}_{1.5}\text{Co}_{1.5}\text{CrFeTi}_{0.5}$  powder (a) morphology (b) cross-section features (SEM, backscattered electron mode).

a combination of both phenomena probably contributed to the observed XRD peaks broadening.

The morphology and cross section of the mechanically alloyed powders are shown in Fig. 2a and b, respectively. As opposed to the XRD results (one BCC and two FCC phases), no distinct different phases contrast could be observed in the powders microstructure (SEM in backscattered electrons mode). Further, no distinguishable chemical composition gradients were observed by EDS mapping. Instead, the powders exhibited a homogenous structure. It could therefore be assumed that the three phases detected by XRD possess close chemical composition. This fact indicated good results of the mechanical alloying process, as it succeeded in production of homogenous alloyed powders

without the need for consecutive annealing. As could be seen from the powder particle cross-section images, the as-milled powders contained oxide inclusions (the small black dots within individual particles in Fig. 2b). Using EDS mapping, these were identified as titanium, chromium, and aluminum oxides and were initially present at the feedstock powder particle surfaces. Eventually, they became dispersed within the milled powder particles as they were trapped inside by the process of repeated cold re-welding and further fracturing when the plasticity of the powder was depleted, i.e. an effect used in case of e.g. ODS (oxide-dispersion strengthened) steels [36].

Due to the repeated powder fracturing and deformation, large strains and defects are introduced to the particles, frequently triggering

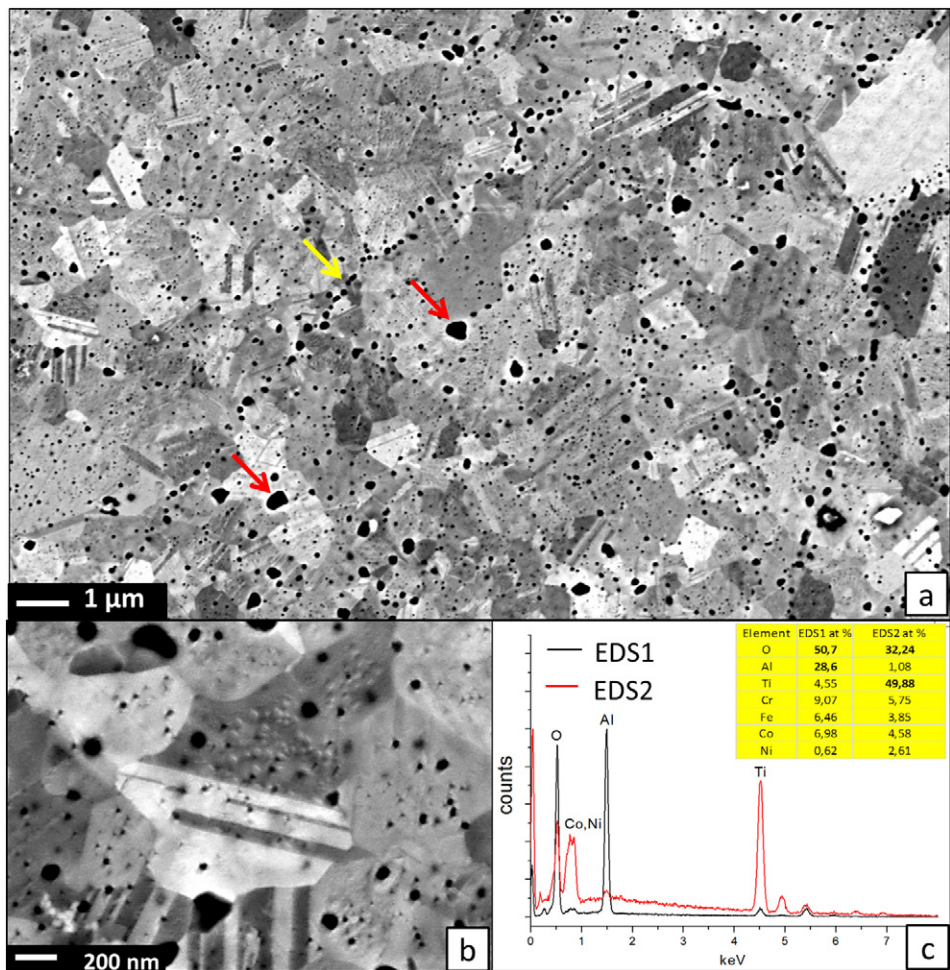


**Fig. 3.** Electron channelling contrast imaging (ECCI) micrographs of (a) the samples after SPS revealing polycrystalline microstructure of the bulk material (red arrows denote sub-micron oxide inclusions, yellow arrow oxide strings at original powder particle boundaries) (b) grains with extremely fine twins (c) example of EDS patterns corresponding to two oxide particles.

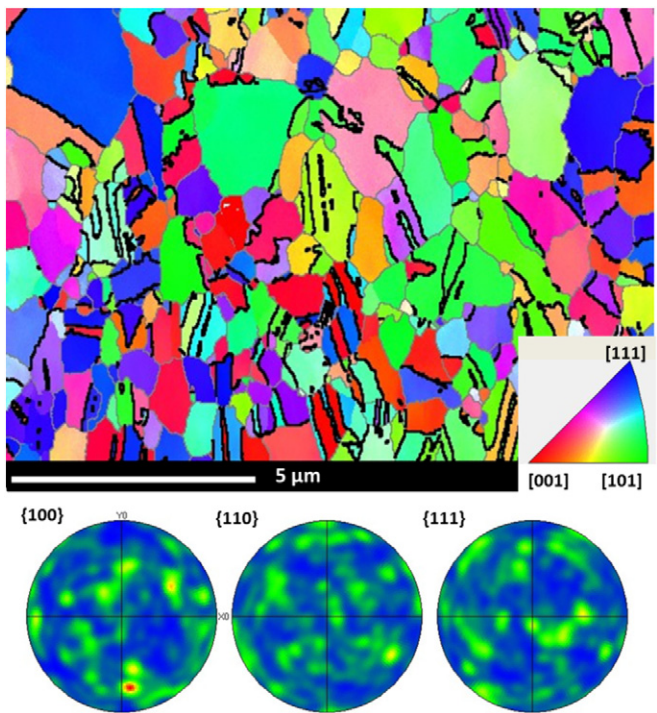


**Fig. 4.** EBSD orientation maps with pole figures showing one phase FCC bulk material with no significant preferred orientation of its grains. Deformation twin boundaries are denoted by wider black lines. Note that the apparent density of the twins appears somewhat lower in the image due to resolution constraints.

a non-equilibrium state in the produced materials [37]. This is referred to as mechanical activation, for this process lowers the necessary activation energy to promote phase changes. Upon high temperature sintering, the phases present in the powders were transformed to single FCC solid solution of all elements with lattice parameter of 3.57 Å, as shown in Fig. 1c. Such transformation is a result of the thermodynamic drive of the material to achieve the most stable state attainable in the present condition (i.e., with the lowest free energy of the system). The phase with the highest stability is characterized by the most negative value of free energy change,  $\Delta G$ . The  $\Delta G$  can be lowered either by increasing the total contribution of the system entropy (one of which is configuration entropy  $\Delta S_{conf}$ ) or lowering the contribution of enthalpy  $\Delta H$  in a well-known equation:

$$\Delta G = \Delta H - T\Delta S \quad (2)$$

where  $T$  is a thermodynamic temperature. Correspondingly, in the case of the alloy produced in this study, the diffusion driven phase transformation to more stable product has been observed. Such transformation was facilitated by the considerably high configuration entropy  $\Delta S_{conf}$  of the solid solution, lowering the total free energy of the solid solution phase, thereby suppressing formation of any ordered intermetallic phases in the respective processing conditions. For any combination of two from the five used elements,  $\Delta H_{mix}$  was not negative enough to

overcome the high configuration entropy of the solid solution phase and cause the precipitation of ordered (intermetallic) compounds, except the oxide inclusions inherited from the initial feedstock.

The powders were SPS consolidated to full density bulks with no apparent porosity distinguishable through SEM analysis. The density measured by the Archimedes method ( $\rho = 7.90 \text{ g} \cdot \text{cm}^{-3}$ ) was higher than the predicted theoretical alloy density of  $7.79 \text{ g} \cdot \text{cm}^{-3}$ , most probably due to the close packing nature of its FCC lattice and the accuracy of the Archimedes method. The microstructure of the samples compacted by SPS is presented in Fig. 3. The microstructure consisted of fine grains of an FCC phase and oxide inclusions. High density of annealing twinning inside the FCC solid solution grains was observed, as also reported in the previous research by Fu et al. [38]. The thickness of most twin lamellae was extremely small, well under 100 nm (Fig. 3b). The twin boundaries could easily be observed from EBSD orientation maps provided in Fig. 4 (denoted by wider black lines). The presence of such nano-twinning suggests low stacking fault energy ( $\gamma_{SFE}$ ) of the FCC solid solution. Considering these, any eventual plastic deformation in the material could be realized by a deformation twinning as an additional mechanism to the prevalent dislocation slip mechanism. The EBSD orientation pole maps presented in Fig. 4 further suggest that, despite the uniaxial pressing during the sintering process, there was no apparent preferred orientation of the FCC phase grains. The average grain size determined from orientation map is  $1.05 \mu\text{m}$ .

Metallic powders exposed to air naturally form oxide shells at their surfaces. The nature of these layers depends on the metal's affinity towards oxygen, time of oxygen/air exposure, and the elemental powder manufacturing process and its purity. During the repeated fracturing and cold re-welding of the original elemental powder particles in the milling process, the oxides present at the particle surfaces form a homogenous dispersion in the cross section of the individual particles. The nature of the oxides (denoted by red and yellow arrows in Fig. 3a) in the produced alloy was identified by EDS analysis as illustrated in the corresponding patterns presented in Fig. 3c for Al, Ti (note that the determined content of oxygen presented in Fig. 3c cannot be considered accurate due to the limitations of the EDS measurement methodology). Aside from individual particles, some of the oxides were arranged in strings, as denoted by the yellow arrow in Fig. 3a. Such feature most probably formed from the oxides present at the original surfaces of the as-milled powder particles prior to the SPS process. During the high temperature sintering, the oxides coagulate to minimize their surface energy (naturally attaining a spherical morphology). The configuration entropy  $\Delta S_{conf}$  of the FCC solid solution phase is insufficient to promote their dissolution, yielding the oxides exceptionally stable and, as such, they were retained in the alloy structure.

The chemical composition of the sintered bulks almost perfectly matched the targeted theoretical values (Table 2), i.e., no selective evaporation of the alloy components took place during the vacuum sintering process.

The single phase FCC microstructure along with the extensive nano-twinning and the presence of extremely small dispersion of oxide inclusions was further confirmed by TEM EDS micro analysis observations and SAED patterning (Fig. 5). The oxides (denoted by red arrows in Fig. 5a) were determined as mostly titanium and aluminum oxides. The former were formed upon contact with ambient atmosphere, given the high affinity of titanium to oxygen. The formation of the latter is a consequence of negligible Al impurity presence in the feedstock powders. Additionally, a little content of chromium oxides was detected only. As demonstrated by the red arrows in Fig. 5b, the oxide inclusions in the SPS compacts frequently served as anchors, pinning down the present dislocation loops, thereby increasing the material yield strength. As the oxides of titanium, chromium and aluminum crystallize in different crystallographic lattices, they generate non-overlapping multiple peaks in the XRD pattern. As such, these phases remain well below the method resolution limit of 5–7 vol.% (i.e., the pertaining peak intensities lie within the spectrum background).

**Table 2**

Theoretical chemical composition of the HEA and composition of the obtained SPS compacted bulks (EDS, atomic %).

Element	Ni	Co	Fe	Cr	Ti
Theoretical composition	27.3	27.3	18.2	18.2	9.1
Bulk after SPS	26.8	27.6	17.4	17.8	9.8

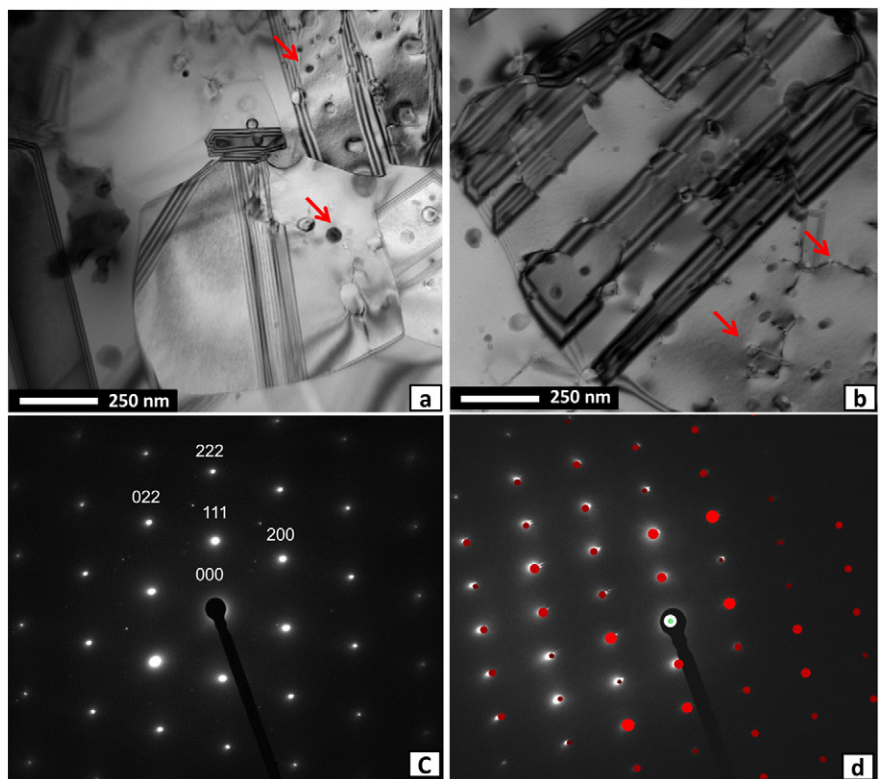


**Fig. 5.** TEM micrographs of (a) FCC grain structure (b) nano-twinning within a single FCC grain. (c) SAED pattern of FCC grain in 110 orientation. (d) SAED pattern of an oxide particle matching the calculated reflections for aluminum oxide. Arrows in Fig. 5a indicate oxide inclusions, arrows in Fig. 5b indicated dislocations pinned at oxide inclusions.

### 3.3. Mechanical behavior

The elastic modulus of the alloy reached as high as 216 GPa, i.e. higher than the calculated average value of the respective used elements (202.7 GPa). Such high value could contribute to superior stiffness of components produced from the material. As the elastic modulus value is proportional to the bonding strength of the atoms, high strength of the metallic bonds within the FCC solid solution could be anticipated. The determined microhardness was 442 HV0.3 (4.335 GPa), i.e. a very high value for a single-phase FCC alloy. This fact could be attributed to the extremely fine grain size and, partially, presence of the fine oxide inclusions that induce Orowan-type strengthening.

The results of the three-point bending test are presented in Table 3, with the representative loading curve provided in Fig. 6. The material exhibited extremely high bending strength  $R_{mb} = 2593$  MPa, and good tensile deformation of 6.89% calculated for tensile stress side of samples. Such exceptional strength is a result of the severe lattice distortion of the high entropy solid solution, with a synergic effect of grain boundary strengthening and a presence of the fine oxide dispersion. Due to the lack of available data in the literature, it is difficult to compare the obtained data with previous research. The only published case of a bending strength test of HEA is in [39], all the values presented in this paper are significantly higher. In fact, they are fully comparable with commonly used high strength alloys, such as tool steels [40,41].

The tensile test results are presented in Table 4 along with the representative engineering stress – engineering strain curve provided in Fig. 7. The elastic modulus determined from the tensile test by fitting the elastic part was 209 GPa. This value is very close to elastic modulus measured by the vibration method (216 GPa) and shows good validity of the obtained results. The alloy has shown a tensile proof stress  $R_{p0.2} = 1308$  MPa, ultimate tensile strength of  $R_m = 1384$  MPa and tensile elongation to fracture  $A_t = 4.01\%$ .

As the most important property for structural part design, yield strength of the fabricated alloy is transparently compared with the data of cast and wrought HEA and MPEA reported in previous studies [42–50] in Fig. 8. For simplicity, all alloys in any way deformed after their casting are referred to as wrought, when in fact they may have undergone homogenization, rolling and annealing processes, just as in the

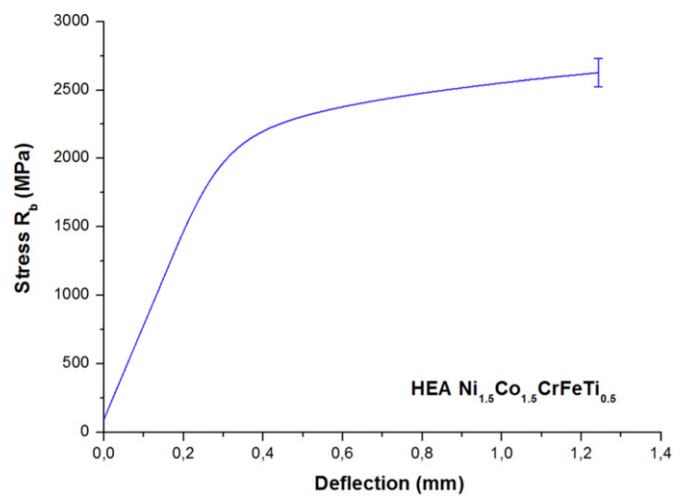


**Fig. 6.** Representative engineering stress – deflection curve from three point bending test.

**Table 3**  
Average three-point bending strength test results.

$R_{mb}$ [MPa]	Maximum deflection [mm]	Work of fracture [ $\text{J} \cdot \text{cm}^{-3}$ ]	Plastic deflection [mm]
2593 ± 102	0.98 ± 0.18	188.2	0.6 ± 0.12

**Table 4**

Average tensile strength test results.

$R_{p0.2}$ [MPa]	$R_m$ [MPa]	Elastic modulus E (GPa)	Elongation to fracture $A_t$ [%]	Strain hardening coefficient [1]
1308	1384	209	4.01	0.11

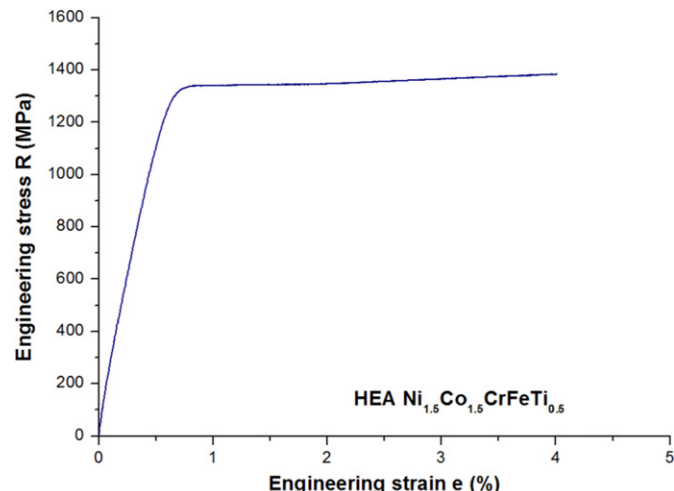


Fig. 7. Engineering stress – strain curve from tensile test.

case of common industrial materials. Apparently, despite its single-phase nature, the combination of high strength and sufficient ductility in the presented alloy is comparable to even the best-performance cast alloys. Given that, it is especially interesting to compare this study results with other single phase alloys.

The fracture surface morphology of the broken bending and tensile test specimens is presented in Fig. 9. High energy ductile fracture mode was observed in both cases, with the oxide particle inclusions present inside some of the individual dimples. The dimple sizes were relatively small, suggesting that the voids nucleation started simultaneously at a number of places, supposedly at the oxide inclusions and

matrix interface boundaries, or intersection sites of the deformation slip bands. Given their respective sizes, the voids growth stage was short, followed by their rapid coalescence and a crack nucleation and propagation, as generally observed in the case of high strength materials. The relatively small strain hardening coefficient during the tensile test ( $n$  equal 0.11 – Table 4) suggests that the alloy microstructure could have been already strengthened prior to testing as a result of the used manufacturing process.

The deformation microstructure of the tensile test specimen directly under the fractured surface presented in Fig. 10 reveals the presence of high density dislocation walls (HDDW – blue arrows) and deformation nano-twins (denoted by red arrows) in selected grains with supposed orientation of (111) planes, in approximately 45° angle to the sample loading direction (yellow double arrow in Fig. 10).

The results presented here demonstrate that HEA can be obtained in five-component  $\text{Ni}_{1.5}\text{Co}_{1.5}\text{CrFeTi}_{0.5}$  system, in accordance with the calculated predictions based on the thermodynamic parameters  $\Delta H_{mix}$ ,  $\Delta S_{conf}$ , and  $\Omega$ . As opposed to the theoretical microstructure prediction based on model by Zhang et al. [12] (theoretically, the alloy microstructure should contain precipitates as its  $\delta > 4\%$ ,  $\Delta H_{mix} \leq -10 \text{ kJ} \cdot \text{mol}^{-1}$  and  $\Delta S_{conf} < 13.38 \text{ J} \cdot \text{mol}^{-1}$ ), the HEA consisted of one FCC phase. Such discrepancy may reside in the fact that the involved calculations inherently contain some simplifying assumptions and may, therefore, be limited in their reliability. Also, these calculations are predictions for perfectly stable phases formed in the as-cast microstructures. In the case of materials produced by PM, the processing temperatures are substantially lower and therefore the diffusion rates may be insufficient.

The sole fact that the alloy presented in this paper contains only single main phase (save for the inherited oxide inclusions) is a solid proof that the selected manufacturing process plays a prominent role in the final microstructure of high entropy materials (cf. multi-phase microstructures observed in the produced  $\text{Ni}_{1.5}\text{Co}_{1.5}\text{CrFeTi}_{0.5}$  cast alloy counterparts [13,26]). The resulting one phase structure presented in this paper is not a result of deliberate metastable processing, bearing in mind the slow cooling from the sintering temperature performed in the hot graphite die in a vacuum (i.e., under significantly reduced heat transfer). However, it is important to note that, as opposed to the casting route, the combination of MA + SPS may be susceptible to producing unstable structures, attributed to lower processing temperatures as in the literature [36]. The reason for suppression of formation of any

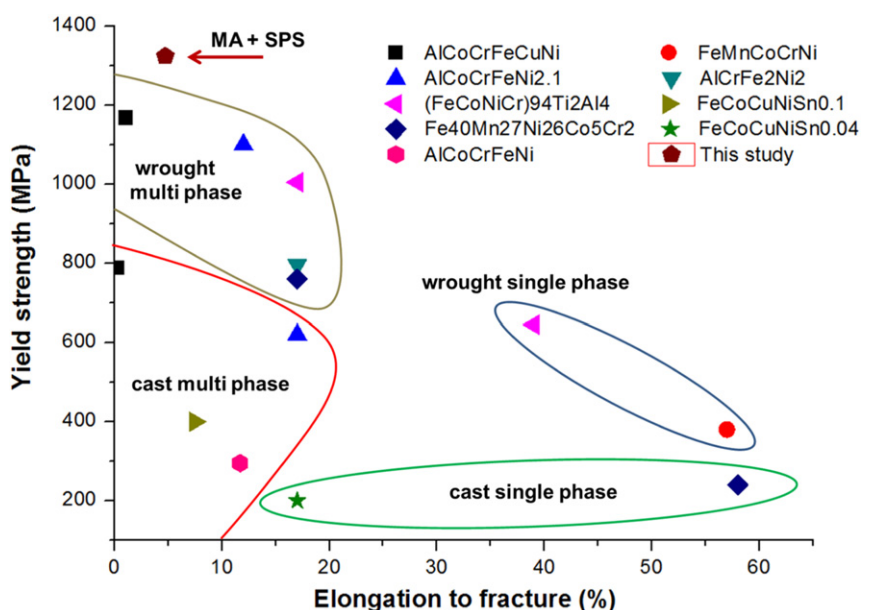
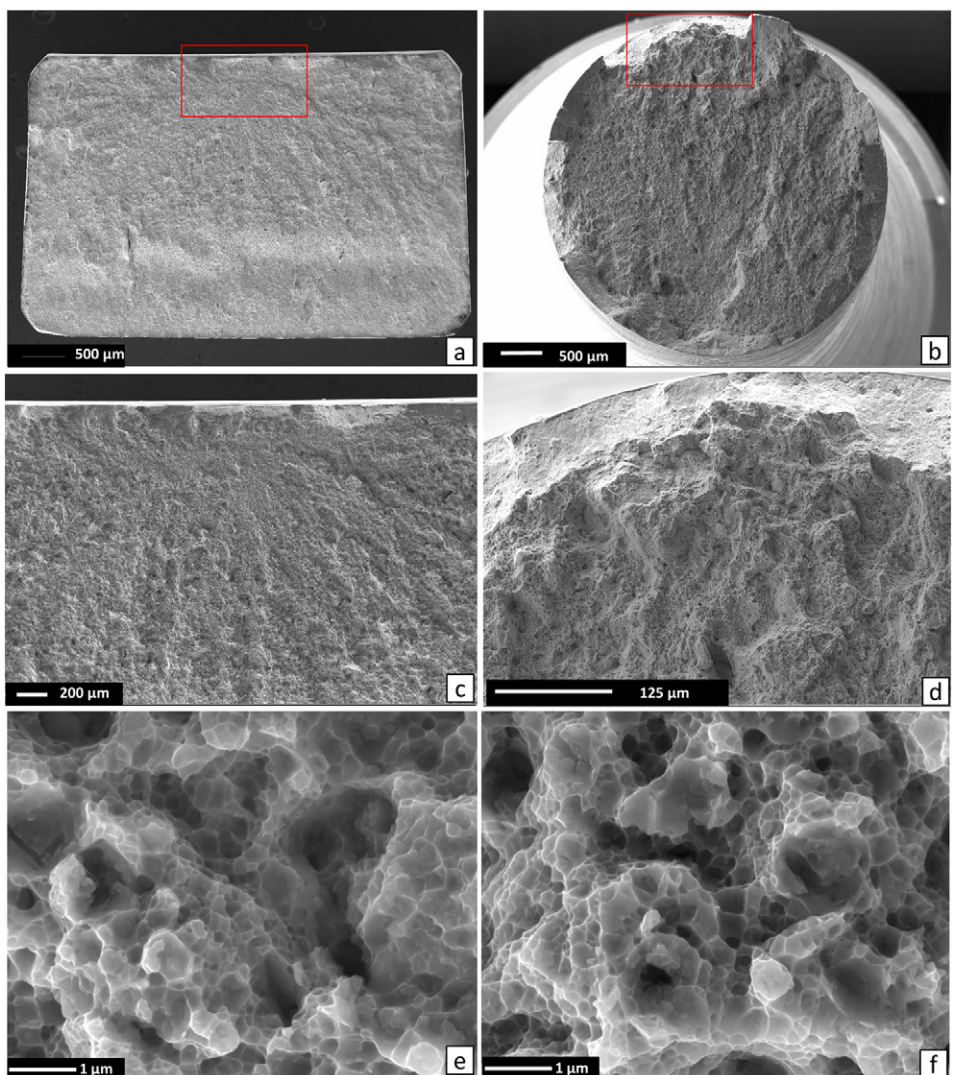
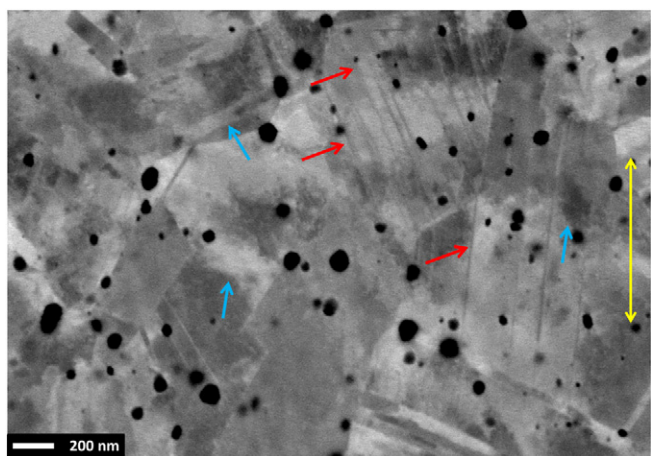


Fig. 8. Engineering yield strength values and elongations to fracture of the SPS compacted alloy presented in this study and different HEA and MPEA alloys with comparable densities produced by traditional casting processes [17,35–42]. Note some of the alloy systems are presented in the figure multiple times as a result of different manufacturing procedure (e.g. as-cast, wrought, annealed etc.).



**Fig. 9.** Typical morphology of fracture surfaces of the samples subjected to (a, c, e) bending test (b, d, f) tensile test.



**Fig. 10.** Deformation microstructure of tensile test specimen in the vicinity of the fractured area. Red arrows indicate deformation nano-twins, blue arrows HDDWs and loading direction denoted by yellow double arrow (SEM ECCI imaging).

intermetallic phases could therefore be either in the lower processing temperature inherent to the PM processing route as previously mentioned before, or in the very slow precipitation kinetics in high entropy solid solutions, that came to be known as sluggish diffusion effect [51]. The formation of ordered intermetallic compounds may result in a beneficial effect on desired properties, especially high temperature strength, but could impair the room temperature ductility. It could also deprive the alloy of the properties believed to be intrinsic to high entropy solid solutions. In fact, having any ordered compounds in the microstructure can significantly reduce the configurational entropy of the adjacent solid solution, therefore decreasing the solid solution strengthening effect. The atomic radii mismatch  $\delta$  in the presented alloy was relatively high (5.04%) compared to other single-phase alloys [10]. Consequently, the amplitude of lattice distortion and solid solution strengthening was very high, potentially yielding a major contribution to the high strength of the pure FCC alloy, comparable to cast double-phase alloys. The alloy exhibited a good combination of superior strength and reasonable ductility, especially for HEA produced by PM route [18–20] (as opposed to alloys with ductility insufficient to perform a valid tensile test). The superior hardness and strengths of the alloy as compared especially to other one phase materials are most probably also the consequence of the observed extreme grain refinement induced by the mechanical alloying process, and the presence of extremely small dispersion of stable oxides. In PM manufacturing

processes, such oxides are inherently formed and their dispersion may play an important role in the mechanical performance of the produced material due to the Orowan strengthening effect by suppressing the dislocation movement and a possibly by retarding grain growth in a high temperature range during sintering and cooling from the sintering temperature. Therefore, the presence of the inclusions can be in a way beneficial for the alloy strength, but detrimental to overall alloy ductility. The deformation in the produced alloy is proposed to be a combination of dislocation slip and deformation twinning. The presence of fine annealing twins in the microstructure prior to any eventual tensile deformation and the presence of deformation twins after such deformation suggested that the stacking fault energy  $\gamma_{SFE}$  of the alloy lies between  $18 < \gamma_{SFE} < 45 \text{ mJ}\cdot\text{m}^{-2}$ , an interval earlier suggested for twins formation [52]. The deformation twining is the prominent toughening mechanism in advanced TWIP steels and also some HEA [53,54]. It is also the main reason for the increase of strength and ductility in FeMnCoCrNi and CoCrNi alloys at cryogenic temperatures [44,54,55]. It promotes the strain hardening capacity, delays the onset of plastic instability and therefore induces simultaneous increase in strength and ductility. In the future research, it could be the key factor for improvement of the tensile ductility of the material.

## 4. Conclusions

In the presented study,  $\text{Ni}_{1.5}\text{Co}_{1.5}\text{CrFeTi}_{0.5}$  high entropy alloy with one phase face centered cubic solid solution structure was successfully synthesized by a combination of mechanical alloying and spark plasma sintering (cf. multi-phase cast alloys produced by traditional casting routes). Excellent combination of mechanical properties was achieved with bend strength  $R_{mb} = 2593 \text{ MPa}$ , tensile strength  $R_m = 1384 \text{ MPa}$ , tensile elongation to fracture of 4.01%, and elastic modulus of 216 GPa. The microhardness of the material reached 442 HV0.3 (4.335 GPa). The result for such good combination of properties can be associated with extreme grain refinement induced by the mechanical alloying process and the lattice distortion effect coupled with oxide particle strengthening. The manufacturing process has a clear influence on the microstructure and properties of the high entropy alloys as compared to cast materials, the change as are most notably connected with increasing strength levels.

## Acknowledgments

Support of Czech Science Foundation project GACR 13-35890S and GACR GB 14-36566G is acknowledged. The research was co-funded by the Ministry of Education, Youth and Sports within the “National Sustainability Programme I” (NETME CENTRE PLUS – LO1202). The authors would like to thank Jan Cupera for his help with SEM analysis.

## References

- [1] J.W. Yeh, S.K. Chen, S.J. Lin, J.Y. Gan, T.S. Chin, T.T. Shun, C.H. Tsau, S.Y. Chang, Nanostructured high-entropy alloys with multiple principal elements: novel alloy design concepts and outcomes, *Adv. Eng. Mater.* 6 (2004) 299–303, <http://dx.doi.org/10.1002/adem.200300567>.
- [2] B. Cantor, I.T.H. Chang, P. Knight, A.J.B. Vincent, Microstructural development in equiatomic multicomponent alloys, *Mater. Sci. Eng. A* 375–377 (2004) 213–218, <http://dx.doi.org/10.1016/j.msea.2003.10.257>.
- [3] O.N. Senkov, G.B. Wilks, J.M. Scott, D.B. Miracle, Mechanical properties of  $\text{Nb}_{25}\text{Mo}_{25}\text{Ta}_{25}\text{W}_{25}$  and  $\text{V}_{20}\text{Nb}_{20}\text{Mo}_{20}\text{Ta}_{20}\text{W}_{20}$  refractory high entropy alloys, *Intermetallics* 19 (2011) 698–706, <http://dx.doi.org/10.1016/j.intermet.2011.01.004>.
- [4] Y. Zhang, T.T. Zuo, Z. Tang, M.C. Gao, K.A. Dahmen, P.K. Liaw, Z.P. Lu, Microstructures and properties of high-entropy alloys, *Prog. Mater. Sci.* 61 (2014) 1–93, <http://dx.doi.org/10.1016/j.pmatsci.2013.10.001>.
- [5] Y.-J. Chang, A.-C. Yeh, The evolution of microstructures and high temperature properties of  $\text{Al}_x\text{Co}_{1.5}\text{CrFeNi}_{1.5}\text{Ti}_y$  high entropy alloys, *J. Alloys Compd.* (2012) 379–385, <http://dx.doi.org/10.1016/j.jallcom.2012.09.042>.
- [6] W.-R. Wang, W.-L. Wang, S.-C. Wang, Y.-C. Tsai, C.-H. Lai, J.-W. Yeh, Effects of Al addition on the microstructure and mechanical property of  $\text{Al}_x\text{CoCrFeNi}$  high-entropy alloys, *Intermetallics* 26 (2012) 44–51, <http://dx.doi.org/10.1016/j.intermet.2012.03.005>.
- [7] Y. Yu, J. Wang, J. Li, H. Kou, W. Liu, Characterization of BCC phases in  $\text{AlCoCrFeNiTi}_x$  high entropy alloys, *Mater. Lett.* 138 (2015) 78–80, <http://dx.doi.org/10.1016/j.matlet.2014.09.100>.
- [8] B.D. Miracle, D.J. Miller, N.O. Senkov, C. Woodward, D.M. Uchic, J. Tiley, Exploration and development of high entropy alloys for structural applications, *Entropy* 16 (2014) <http://dx.doi.org/10.3390/e16010494>.
- [9] U. Roy, H. Roy, H. Daoud, U. Glatzel, K.K. Ray, Fracture toughness and fracture micromechanism in a cast  $\text{AlCoCrCuFeNi}$  high entropy alloy system, *Mater. Lett.* 132 (2014) 186–189, <http://dx.doi.org/10.1016/j.matlet.2014.06.067>.
- [10] Z. Wu, H. Bei, F. Otto, G.M. Pharr, E.P. George, Recovery, recrystallization, grain growth and phase stability of a family of FCC-structured multi-component equiatomic solid solution alloys, *Intermetallics* 46 (2014) 131–140, <http://dx.doi.org/10.1016/j.intermet.2013.10.024>.
- [11] B. Schuh, F. Mendez-Martin, B. Völker, E.P. George, H. Clemens, R. Pippan, A. Hohenwarter, Mechanical properties, microstructure and thermal stability of a nanocrystalline  $\text{CoCrFeMnNi}$  high-entropy alloy after severe plastic deformation, *Acta Mater.* 96 (2015) 258–268, <http://dx.doi.org/10.1016/j.actamat.2015.06.025>.
- [12] K. Zhang, Z. Fu, Effects of annealing treatment on phase composition and microstructure of  $\text{CoCrFeNiTiAl}_x$  high-entropy alloys, *Intermetallics* 22 (2012) 24–32, <http://dx.doi.org/10.1016/j.intermet.2011.10.010>.
- [13] M.-H. Chuang, M.-H. Tsai, W.-R. Wang, S.-J. Lin, J.-W. Yeh, Microstructure and wear behavior of  $\text{Al}_x\text{Co}_{1.5}\text{CrFeNi}_{1.5}\text{Ti}_y$  high-entropy alloys, *Acta Mater.* 59 (2011) 6308–6317, <http://dx.doi.org/10.1016/j.actamat.2011.06.041>.
- [14] D. Li, Y. Zhang, The ultrahigh charpy impact toughness of forged  $\text{AlxCrFeNi}$  high entropy alloys at room and cryogenic temperatures, *Intermetallics* 70 (2016) 24–28, <http://dx.doi.org/10.1016/j.intermet.2015.11.002>.
- [15] C. Ng, S. Guo, J. Luan, Q. Wang, J. Lu, S. Shi, C.T. Liu, Phase stability and tensile properties of co-free  $\text{Al}_0.5\text{CrCuFeNi}_2$  high-entropy alloys, *J. Alloys Compd.* 584 (2014) 530–537, <http://dx.doi.org/10.1016/j.jallcom.2013.09.105>.
- [16] N.D. Stepanov, N.Y. Yurchenko, V.S. Sokolovsky, M.A. Tikhonovsky, G.A. Salishchev,  $\text{AlNbTiVZr}_{0.5}$  high-entropy alloy combining high specific strength and good ductility, *Mater. Lett.* (2015), <http://dx.doi.org/10.1016/j.matlet.2015.08.099>.
- [17] Z. Fu, W. Chen, S. Fang, X. Li, Effect of Cr addition on the alloying behavior, microstructure and mechanical properties of twinned  $\text{CoFeNiAl}_{0.5}\text{Ti}_{0.5}$  alloy, *Mater. Sci. Eng. A* 597 (2014) 204–211, <http://dx.doi.org/10.1016/j.msea.2013.12.096>.
- [18] W. Chen, Z. Fu, S. Fang, H. Xiao, D. Zhu, Alloying behavior, microstructure and mechanical properties in a  $\text{FeNiCrCo}_{0.3}\text{Al}_{0.7}$  high entropy alloy, *Mater. Des.* 51 (2013) 854–860, <http://dx.doi.org/10.1016/j.matdes.2013.04.061>.
- [19] Z. Fu, W. Chen, H. Xiao, L. Zhou, D. Zhu, S. Yang, Fabrication and properties of nanocrystalline  $\text{Co}_{0.5}\text{FeNiCr}_{0.5}$  high entropy alloy by MA-SPS technique, *Mater. Des.* 44 (2013) 535–539, <http://dx.doi.org/10.1016/j.matdes.2012.08.048>.
- [20] E. Jajarmi, L. Desogus, R. Orrù, S.A. Sajjadi, G. Cao, On the fabrication of functional graded 3YPSZ/316L materials by SPS: Process optimization and characterization of the obtained products, *Ceramics International* 42 (7) (2016) 8351–8359, <http://dx.doi.org/10.1016/j.ceramint.2016.02.050>.
- [21] S. Praveen, B.S. Murty, R.S. Kottada, Alloying behavior in multi-component  $\text{AlCoCrFeNi}$  and  $\text{NiCoCrFeNi}$  high entropy alloys, *Mater. Sci. Eng. A* 534 (2012) 83–89, <http://dx.doi.org/10.1016/j.msea.2011.11.044>.
- [22] I. Moravcik, J. Cizek, P. Gavendova, S. Sheikh, S. Guo, I. Dlouhy, Effect of heat treatment on microstructure and mechanical properties of spark plasma sintered  $\text{AlCoCrFeNiTi}_{0.5}$  high entropy alloy, *Mater. Lett.* 174 (2016) 53–56, <http://dx.doi.org/10.1016/j.matlet.2016.03.077>.
- [23] G. Zhu, Y. Liu, J. Ye, Fabrication and properties of Ti(C,N)-based cermets with multi-component  $\text{AlCoCrFeNi}$  high-entropy alloys binder, *Mater. Lett.* 113 (2013) 80–82, <http://dx.doi.org/10.1016/j.matlet.2013.08.087>.
- [24] J. Leunda, C. Soriano, C. Sanz, V.G. Navas, Laser cladding of vanadium-carbide tool steels for die repair, *Phys. Procedia* 12 (2011) 345–352, <http://dx.doi.org/10.1016/j.phpro.2011.03.044> (Part A).
- [25] R.O. Ritchie, The conflicts between strength and toughness, *Nat. Mater.* 10 (2011) 817–822, <http://dx.doi.org/10.1038/nmat3115>.
- [26] Y.L. Chou, J.W. Yeh, H.C. Shih, The effect of molybdenum on the corrosion behaviour of the high-entropy alloys  $\text{Co}_{1.5}\text{CrFeNi}_{1.5}\text{Ti}_{0.5}\text{Mo}_x$  in aqueous environments, *Corros. Sci.* 52 (2010) 2571–2581, <http://dx.doi.org/10.1016/j.corsci.2010.04.004>.
- [27] A.-C. Yeh, Y.-J. Chang, C.-W. Tsai, Y.-C. Wang, J.-W. Yeh, C.-M. Kuo, On the solidification and phase stability of a Co-Cr-Fe-Ni-Ti high-entropy alloy, *Metall. Mater. Trans. A* 45 (2013) 184–190, <http://dx.doi.org/10.1007/s11661-013-2097-9>.
- [28] S. Zaeferer, N.-N. Elhami, Theory and application of electron channelling contrast imaging under controlled diffraction conditions, *Acta Mater.* 75 (2014) 20–50, <http://dx.doi.org/10.1016/j.actamat.2014.04.018>.
- [29] ISO 6892 - 1, The Tensile Strength Test was Performed Using 2 Metallic Materials – Tensile Testing – Part 1: Method of Test at Room Temperature, 2009.
- [30] M. Umemoto, K. Tsuchiya, Z.G. Liu, S. Sugimoto, Tensile stress-strain analysis of single-structure steels, *Mettal. Mater. Trans. A* 31 (2000) 1785–1794, <http://dx.doi.org/10.1007/s11661-006-0249-x>.
- [31] ASTM E1876 - 15, Standard Test Method for Dynamic Young's Modulus, Shear Modulus, and Poisson's Ratio by Impulse Excitation of Vibration, ASTM International, West Conshohocken, PA, 2015, <http://dx.doi.org/10.1520/E1876-15>.
- [32] Y. Zhang, Y.J. Zhou, J.P. Lin, G.L. Chen, P.K. Liaw, Solid-solution phase formation rules for multi-component alloys, *Adv. Eng. Mater.* 10 (2008) 534–538, <http://dx.doi.org/10.1002/adem.200700240>.
- [33] X. Yang, Y. Zhang, Prediction of high-entropy stabilized solid-solution in multi-component alloys, *Mater. Chem. Phys.* 132 (2012) 233–238, <http://dx.doi.org/10.1016/j.matchemphys.2011.11.021>.
- [34] S. Guo, Q. Hu, C. Ng, C.T. Liu, More than entropy in high-entropy alloys: forming solid solutions or amorphous phase, *Intermetallics* 41 (2013) 96–103, <http://dx.doi.org/10.1016/j.intermet.2013.05.002>.